



Bio-template synthesis of Mo-doped polymer carbon nitride for photocatalytic hydrogen evolution

Yanyun Wang, Yiwei Zhang*, Shuo Zhao, Ziwei Huang, Wenxia Chen, Yuming Zhou*, Xushuai Lv, Shenhao Yuan

School of Chemistry and Chemical Engineering, Southeast University, Jiangsu Optoelectronic Functional Materials and Engineering Laboratory, Nanjing, 211189, PR China



ARTICLE INFO

Keywords:

Biological template
Mo-doped $g\text{-C}_3\text{N}_4$
Chelation
Receptor-donor built-in electric field
Photocatalytic hydrogen evolution

ABSTRACT

Herein, a novel strategy is established to synthesize Mo-doped graphitic carbon nitride ($g\text{-C}_3\text{N}_4$) with excellent photocatalytic activity through a green approach of biological template. The addition of biotemplates provides a microenvironment for the formation of hydrogen bonds in which the flower-like $g\text{-C}_3\text{N}_4$ is formed by self-assembly between precursors, which not only increases the specific surface area of the material but also exposes more catalytic activity edge. Benefiting from the non-localized of Mo(VI) 4d orbital, Mo-doped $g\text{-C}_3\text{N}_4$ constructs a suitable band structure and a built-in electric field that promotes electron delocalization, which improves the absorption range of visible light and separation efficiency of photo-generated electron-hole pairs. Subsequently, a possible chelation-hydrogen bond coordination mechanism was proposed based on the characterization results of X-ray diffraction (XRD), X-ray photoelectron spectroscopy (XPS), electron paramagnetic resonance (EPR) and ^{15}N solid-state NMR (^{15}N NMR). As a result, the π -conjugated system of $g\text{-C}_3\text{N}_4$ was extended by forming a chelate centered on Mo(VI). Photocatalytic hydrogen evolution (PHE) showed that the optimal hydrogen evolution rate of Mo-doped $g\text{-C}_3\text{N}_4$ was as high as 2008.9 $\mu\text{mol/g}\cdot\text{h}$, which was 9.6 times than that of bulk $g\text{-C}_3\text{N}_4$.

1. Introduction

The development of technology and economy is inseparable from the demand of energy. Correspondingly, the contradiction between the sharp consumption of fossil fuels and the protection of environment becomes more and more prominent, so the development of sustainable energy is imminent [1,2]. Hydrogen, as a kind of high-calorie value, environmentally-friendly green energy has gained considerable attention in the past few decades. Photocatalytic technology is expected to achieve sustainable energy production under the premise of fully utilizing solar energy, showing great potential in energy and environment.

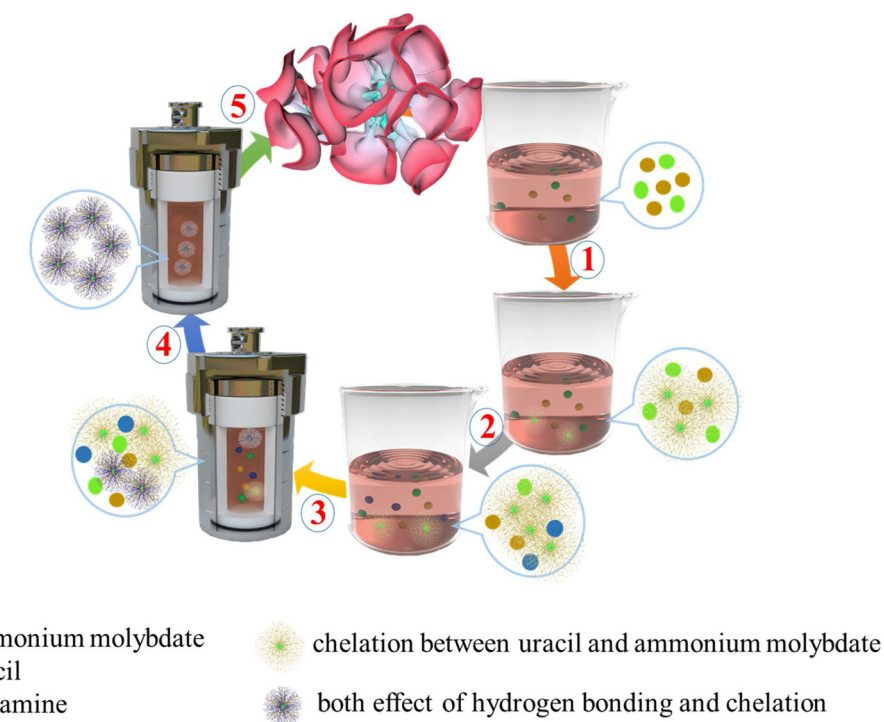
Photocatalytic hydrogen evolution has emerged as an ideal green technology for converting solar energy into clean energy, and extensive efforts have been put to develop various catalysts to improve the utilization of sunlight. Among them, Polymer carbon nitride has attracted much attention because of its unique properties, such as abundance of raw materials, excellent photochemical stability and reasonable costs [3]. However, the practical application of bulk $g\text{-C}_3\text{N}_4$ is challenged by its inherent limitation of low quantum yield, rapid charge recombination, low conductivity, and low utilization of visible light, leading to unsatisfactory results in application [4]. From this point of view,

various modification schemes including morphology control, band gap regulation and defect engineering have been developed to overcome the self-defect of the bulk $g\text{-C}_3\text{N}_4$ [5,6]. For example, Wang and her team prepared a $g\text{-C}_3\text{N}_4@\text{TiO}_2$ core-shell photocatalyst using a method of sol-gel in-situ coating reassembly in which the thickness of the ultra-thin $g\text{-C}_3\text{N}_4$ layer was controllable. Relatively, Liu et al. reported a wide-range photoresponse O-substituted $g\text{-C}_3\text{N}_4$ with tunable band structure and effective separation of photogenerated charge through one-pot co-pyrolysis of melamine and substantial ammonium acetate. Correspondingly, Che and his co-workers obtained ultra-thin $ug\text{-C}_3\text{N}_4$ nanosheets with large specific surface area and nitrogen-rich vacancies through NO_3^- intercalation mechanism [7–9]. In general, these methods have greatly improved the activity of $g\text{-C}_3\text{N}_4$. However, in order to promote the wide application of $g\text{-C}_3\text{N}_4$, it is also necessary to explore other modifications for further optimization of photocatalytic performance.

Metal functionalization and biomimetic mineralization are two common natural phenomena. It is worth noting that metal functionalization can effectively improve the spectral absorption of organometallic complexes and promote the transfer of photogenerated electrons [10]. Interestingly, biomimetic mineralization can not only regulate the size and morphology of inorganic materials by virtue of the microenvironment

* Corresponding authors.

E-mail addresses: zhangchem@seu.edu.cn (Y. Zhang), ymzhou@seu.edu.cn (Y. Zhou).



Scheme 1. Schematic illustration of the synthetic procedure used to prepare Mo-doped $\text{g-C}_3\text{N}_4$.

provided by biomolecules, but also increase the specific surface area of the catalyst by self-assembly between molecules [11]. Inspired by natural biomimetic mineralization and metal functionalization, we synthesized Mo-doped $\text{g-C}_3\text{N}_4$ using uracil as a biological template and ammonium molybdate as a molybdenum source. Benefiting from the formation potential for hydrogen bonding between biological templates and other molecules, flower-shaped $\text{g-C}_3\text{N}_4$ was prepared by self-assembly between precursors. At the same time, the Mo(VI)-centered chelate was formed in the hydrothermal process. On the one hand, the empty orbital of Mo(VI) acts as an electron acceptor to accept electrons from the pyrimidine ring donor, thereby promoting the transfer of photo-generated electrons. On the other hand, the formation of the chelate ensured that Mo(VI) was successfully embedded in the $\text{g-C}_3\text{N}_4$ skeleton. Besides, the detailed synthesis process is illustrated in **Scheme 1**.

2. Experimental

2.1. Hydrothermal preparation of catalysts

Mo-doped $\text{g-C}_3\text{N}_4$ was synthesized as follows: 30 mg of uracil (Sinopharm Chemical Reagent Co. Ltd) and a certain mass percentage (0.1%, 0.2% and 0.3% relative to melamine to be added later) of ammonium molybdate (Sinopharm Chemical Reagent Co. Ltd) were dissolved in 30 mL of deionized water to form a homogeneous solution. Subsequently, 2 g of melamine (Shanghai Lingfeng Chemical Reagent Co. Ltd) was added to the above suspension and stirred for another 6 h. Then, the resulting solution was transferred to a 50 mL Teflon-lined stainless steel autoclave and kept at 200 °C for 12 h. After cooling to room temperature, the mixture was collected and dried in a vacuum oven at 80 °C for 24 h. Finally, the white solid was placed in a tube furnace and annealed at 550 °C for 4 h under a nitrogen atmosphere with a heating rate of 2.3 °C/min. The obtained solid powder was labeled as $\text{CN-Mo}_{0.1}$, $\text{CN-Mo}_{0.2}$ and $\text{CN-Mo}_{0.3}$, respectively. For comparison, pure $\text{g-C}_3\text{N}_4$ was prepared in the same manner without addition of uracil and ammonium molybdate, and the yellow product was labeled as CN .

2.2. Instruments and measurements

Crystal structures of the samples were performed on X-ray powder diffraction (XRD, Bruker D8 Advance, $\lambda = 1.5418 \text{ \AA}$). Fourier-transform infrared (FT-IR) spectra were acquired on a Bruker ALPHA-T FT-IR spectrometer. The UV-vis diffuse reflectance spectra were conducted using UV/Vis-NIR spectrophotometer (Shimadzu UV-3600) with BaSO_4 as the reference substance, then converted into absorption spectra by Kubelka-Munk transformation. The scanning electron microscopy (SEM, JSM-6700 F, 5 kV) was carried out to observe morphologies of the as-prepared samples. Transmission electron microscopy (TEM) and high resolution transmission electron microscope (HRTEM) were conducted on a JEOL JEM-1010 electron microscope operating at an accelerating voltage of 200 kV. X-ray photoelectron spectroscopy (XPS) spectra were obtained using a Thermo VG Scientific Escalab 250 spectrometer. All binding energies were referred to the C 1 s peak of the surface adventitious carbon at 284.8 eV. ^{15}N solid state nuclear magnetic resonance (^{15}N NMR) spectroscopy was collected on a Bruker Avance III HD NMR spectrometer, which was cross-polarized at a magic angular rotation speed of 10.0 kHz with a cross-polarization time of 2 ms and a cycle delay time of 5 s. Electron paramagnetic resonance (EPR) was tested on an EPR spectrometer (JES-FA 200, JEOL) with a microwave power of 1.0 mW to observe the separation of electron-hole pairs. Ultraviolet photoelectron spectroscopy (UPS-ESCALAB 250Xi, America) measurements were carried out with an unfiltered He I (21.22 eV) gas discharge lamp to calculate the valence band potential. Brunauer-Emmett-Teller (BET) nitrogen adsorption-desorption was measured at 77 K on a Micrometrics ASAP 2020 system. The photoluminescence (PL) and time-resolved fluorescence decay spectra were monitored with a Shimadzu RF-5301 at room temperature under the excitation of 365 nm. Thermogravimetric (TG) analysis was performed by an integrated thermal analyzer with a heating rate of 20 °C/min in N_2 .

2.3. Photoelectrochemical measurements

Photoelectrochemical measurements were carried out in a

conventional three-electrode electrochemical workstation with 0.1 M Na₂SO₄ aqueous solution as the electrolyte. Typically, the FTO glass coated with photocatalyst was used as working electrode, Pt wire and saturated calomel electrode were acted as counter and reference electrode, respectively. The 300 W Xe lamp with 420 nm cutoff filter was used as visible light source. The working electrodes were prepared as follows: 10 mg sample was dispersed in a mixed solution of ethanol (1 mL) and Nafion solution (10 μL), and the resulting solution was ultrasonicated for 30 min. Then, 30 μL of the above mixed droplets were transferred onto a 0.5 cm² FTO glass electrode. Finally, the prepared electrodes were dried at 200 °C for 2 h.

2.4. Evaluation of photocatalytic activity

The experiments of photocatalytic H₂ evolution were carried out in a gas circulation system (LbSolar-3AG, Perfect Light, Beijing). For each experiment, 50 mg of photocatalyst powder was mixed in 100 mL aqueous solution in the presence of 10 Vol.% triethanolamine as sacrificial reagent. 3 wt% Pt as co-catalyst was loaded by *in situ* photodeposition to boost hydrogen evolution. Visible light was served by a Xe lamp (300 W) equipped with 420 nm and 460 nm cutoff filter, respectively. Before irradiation, the suspension was evacuated several times to remove air completely. The reaction temperature was maintained at 6 °C by a flow of cooling recycling water. The generated hydrogen was measured by an online gas chromatograph equipped with a thermal conductivity detector (TCD, 5 Å molecular sieve column) using argon as carrier gas. The apparent quantum efficiency (AQE) of the samples was calculated by monochromatic photoexcitation ($\lambda = 420$ nm, $\lambda = 460$ nm) under the same experimental conditions, and the formula is as follows:

$$AQE = \frac{2 \times \text{number of evolved H}_2 \text{ molecules}}{\text{number of incident photons}} \times 100\%$$

3. Results and discussion

3.1. Characterization of the catalysts

Phase information about the synthesized materials was explored by powder XRD. As presented in Fig. 1a, two distinct diffraction peaks of in-plane packing (100) and interfacial stacking (002) confirmed the successful formation of g-C₃N₄. In detail, the strong peak 27.1° is attributed to the interlayer stacking of periodic tris-s-triazine units, while the peak at 13.2° corresponds to the trigonal N linkage of the aromatic structure in-plane repeat motif [12,13]. Notably, the obvious shift occurred in the (002) diffraction peak of the catalysts modified by ammonium molybdate (Fig. 1b), which might be related to the lattice distortion of g-C₃N₄ caused by Mo(VI) doping. Clearly, no diffraction peaks related to Mo species were observed except for the characteristic peaks of g-C₃N₄, which means that the incorporation of Mo did not produce a new crystalline phase, and traces of Mo was well dispersed in the catalysts system.

FT-IR experiment was carried out to elucidate the chemical structure of the synthesized samples. From Fig. 1c, the reverse peak at 805 cm⁻¹ is attributed to the CN stretching vibration of the triazine heterocycle, and a number of strong peaks between 1200 and 1700 cm⁻¹ correspond to the characteristic vibrational peaks of the heptazine derivative, including stretching vibrations of C=N–C and C–N skeleton vibrations of the aromatic heterocycle [14,15]. Generally, the broad peak at 3000–3500 cm⁻¹ is derived from the surface adsorbed hydroxyl groups and some free amino groups, predicting that some water molecules may be attached to the catalyst surface and some of the exposed nitrogen atoms in the system are partially hydrogenated [16]. It is worth noting that the Mo-doped samples exhibit an enhanced asymmetric stretching vibration of the cyano functional group (–C≡N) at 2167 cm⁻¹ compared to the original CN, which may correspond to

the distinctive of carbon environment in the framework due to the successful insertion of Mo(VI).

The photoresponsive properties of all samples were investigated by UV/Vis diffuse reflectance spectroscopy. During the process, electrons are transferred from the valence band (VB) filled by the N 2p orbital to the conduction band (CB) formed by the C 2p orbital. As a result, the CN exhibits a typical semiconductor absorption in which the absorption edge is near 460 nm (Fig. 1d). Compared to CN, the samples of CN-Mo_x (X represents the percentage of ammonium molybdate) exhibit stronger absorption for visible light and significant red shift, which may be assigned to the fact that the doping energy level of Mo⁶⁺ ions is lower than CB [17]. Moreover, this phenomenon can be visually reflected from the color change of the as-obtained samples (Fig. S1).

SEM was applied to investigate microscopic morphology of the as-obtained samples. As presented in Fig. 2a, CN exhibits a rod-like structure after hydrothermal treatment, in which the connections are disordered. However, with the addition of uracil and ammonium molybdate, the microstructure of the catalyst changes significantly. The complex self-assembly between the precursors allows the catalysts to exhibit a variety of flower-like structures that are different from pure CN (Fig. 2b-d). The energy-dispersive X-ray spectroscopy (EDS) mapping was used to measure the distribution and content of elements. As shown in Fig. 2e–g, elemental C, N and Mo are distributed uniformly in CN-Mo_{0.2}. Accordingly, the specific percentages of C, N and Mo in CN-Mo_{0.2} are shown in Table 1. Furthermore, the EDS spectrum (Fig. 2h) obtained from the sample of CN-Mo_{0.2} is considered to be the preliminary evidence for the successful doping of Mo(VI). Consequently, we can obtain the similar morphological information of CN (Fig. S2a) and CN-Mo_{0.2} (Fig. S2c) from TEM images. As shown in Fig. S2b, no lattice fringes were observed in the HRTEM of the bulk g-C₃N₄, which may be attributed to its poor crystallinity. Interestingly, lattice fringes with 0.322 nm distance appeared at the edge of CN-Mo_{0.2} (Fig. S2d), corresponding to the periodic stacking of its (002) crystal plane. The appearance of lattice fringes may be attributed to the doping of Mo(VI) improving the crystallinity of the material. In contrast, no new crystalline phase associated with the Mo species was observed in the selected area electron diffraction pattern of CN-Mo_{0.2}, therefore, the Mo (VI) may be doped into the polymer framework.

XPS was studied to determine the chemical state of the Mo phase generated in the sample during carbonization. As depicted in Fig. 3a, a weak peak attributed to Mo 3d was observed in CN-Mo_{0.2} after the addition of ammonium molybdate. Moreover, the high resolution spectral regions of N 1s, C 1s, Mo 3d and O 1s were obtained. For CN, the high-resolution spectrum of N 1s (Fig. 3b) can be fitted into four peaks, related to C=N=C (398.7 eV) formed by sp² hybridization, N–(C)3 (399.9 eV) in the tertiary nitrogen state, C–N–H(400.9 eV) bond and charging effect (404.5 eV), respectively [18–20]. Compared to CN, the four convolution peak positions of N 1s in CN-Mo_{0.2} move toward higher binding energy, which may result from the interaction between N and Mo(VI) [21]. Similarly, the high-resolution spectral signal of C 1s (Fig. 3c) can be deconvoluted into three peaks with binding energies at 284.6, 286.7, and 288.2 eV, corresponding to the C–C bond from the adventitious carbon, C–NH₂ in the carbon nitride framework and sp²-hybridized N=C=N, respectively [22]. For CN-Mo_{0.2}, the area of the C–NH₂ convolution peak is significantly increased except for the shifting with corresponding convolution peaks, which may be due to the incomplete release of N element in ammonium molybdate during polymerization. Two distinct characteristic peaks of Mo(VI) 3d_{3/2} (235.2 eV) and Mo(VI) 3d_{5/2} (232.1 eV) were observed in the Mo 3d spectrum (Fig. 3d), indicating that the main form of Mo in the g-C₃N₄ skeleton was +6 state (Mo⁶⁺), and a small amount of Mo existed in the form of Mo⁴⁺ (230.0 eV) [23,24]. Since a large amount of NH₃ is released during calcination, the presence of Mo⁴⁺ may be attributed to the reduction of a small amount of Mo⁶⁺ exposed to the surface of the catalyst. Moreover, the binding energy of Mo(VI)3d_{3/2} and Mo(VI) 3d_{5/2} in molybdc acid (MoO₄²⁻) are located at 235.8 eV and 232.7 eV,

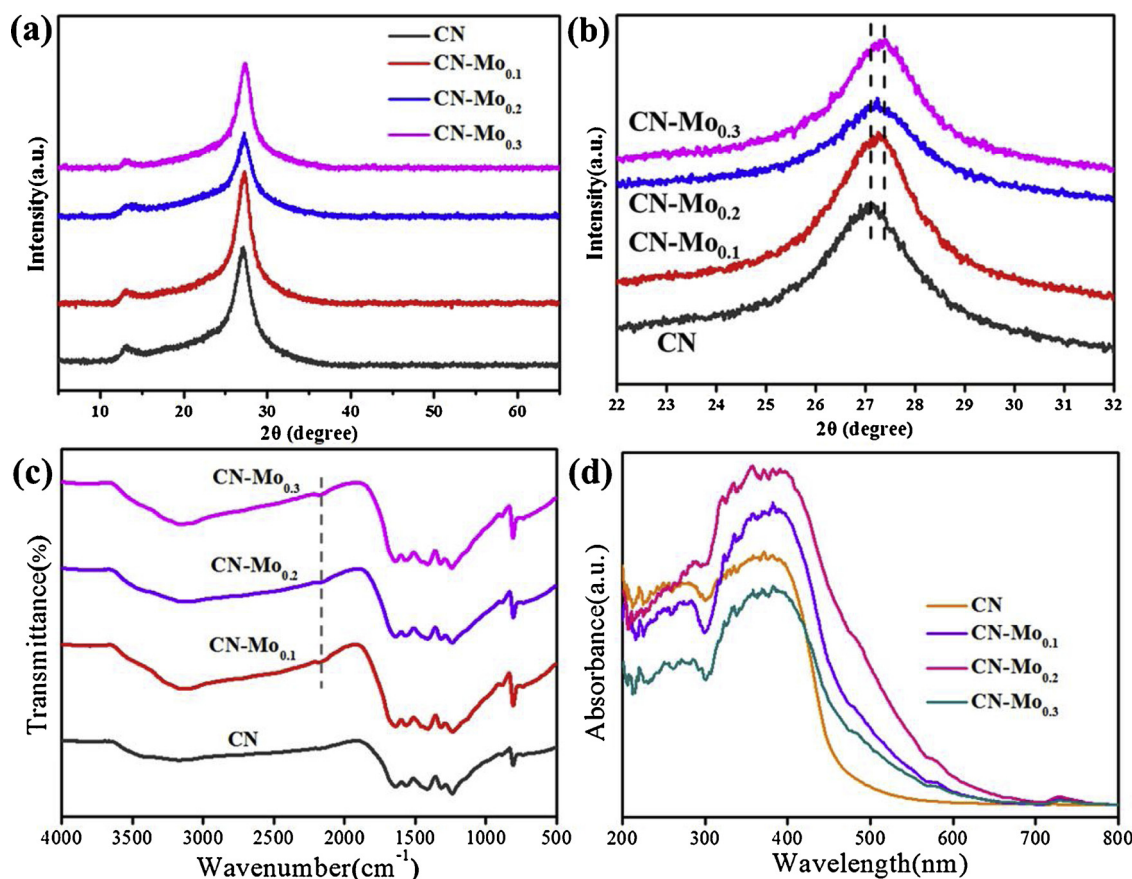


Fig. 1. (a) XRD patterns; (b) shift corresponding to (002) diffraction peak of the as-prepared samples; (c) FT-IR spectra of the pristine CN, CN-Mo_{0.1}, CN-Mo_{0.2}, CN-Mo_{0.3}; (d) UV-vis diffuse reflectance spectrum.

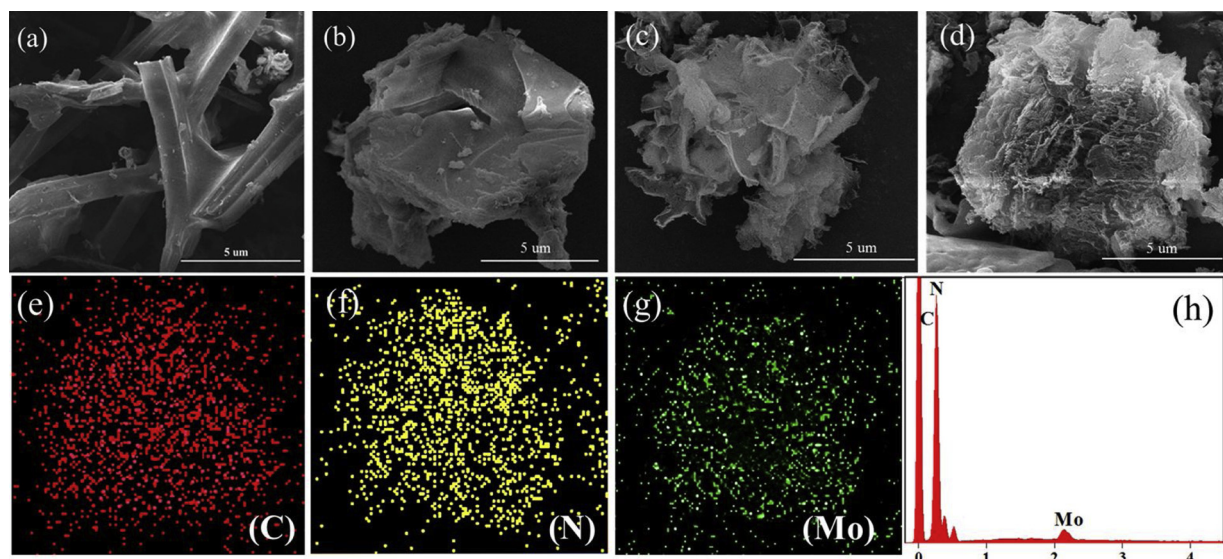


Fig. 2. Typical SEM images of (a) CN; (b) CN-Mo_{0.1}; (c) CN-Mo_{0.2}; (d) CN-Mo_{0.3}; corresponding EDS mapping images of (e) C, (f) N, (g) Mo for CN-Mo_{0.2}; (h) EDS spectrum of CN-Mo_{0.2}.

respectively [25]. Compared with this, the corresponding peaks in Fig. 3d move to a lower binding energy by 0.6 eV, which may be due to the bonding of Mo(VI) to the N atom with a lower electronegativity than the O atom. The peak shown in Fig. 3e with a binding energy of 531.5 eV in O 1 s spectrum corresponds to an oxidized surface group of the carbon substrate. However, no peaks of Mo–O bonds assigned to the MoO₃ phase at ~530.7 eV were observed in the O 1 s spectra of CN-

Mo_{0.2}, suggesting that no oxide phase associated with Mo was formed [26]. As a consequence, the Mo(VI) was successfully bonded to the framework of g-C₃N₄. The TG evaluation of CN and CN-Mo_{0.2} was operated in a nitrogen atmosphere to assess the thermal stability of the samples. As depicted in Fig. 3f, with the increasing of temperature, the CN experienced significant weight loss due to oxidation of the periodic framework, and the tris-triazine structure was fully carbonized at

Table 1
Percentage of elements in CN-Mo_{0.2}.

Element	Weight (%)	Atomic (%)
C K	31.52	36.78
N K	65.36	62.65
Mo L	3.12	0.57
Totals	100.00	100.00

730 °C [27]. In contrast, the reduced thermal stability of the CN-Mo_{0.2} causes it to decompose at a lower temperature of 430 °C, which is mainly due to its brittle porous structure. At the same time, the presence of Mo(VI) ensures that the CN-Mo_{0.2} is not completely decomposed at a temperature of 665 °C.

¹⁵N solid state NMR spectroscopy was used to analyze the chemical structure of the material in detail. The analytical signal of different nitrogen atoms can be obtained by the principle of coupled full polarization. Three sets of similar formants appeared in the ¹⁵N solid state NMR spectrum (Fig. 4) of polymer CN and CN-Mo_{0.2}, the peak at around 182 ppm is assigned to the peripheral tertiary nitrogen on the heptazine ring. The peaks of 128 ppm and 108 ppm are attributed to the secondary amino (NH) bridging group and the terminal amine (NH₂), respectively [22,28]. The appearance of the secondary bridging NH signal directly represents the formation of a heptazine ring polymerization framework [29]. Interestingly, we observed a significant increase in the peak area of NH₂ in CN-Mo_{0.2}, which means that CN-Mo_{0.2} has a larger polymer chain length and an enhanced degree of polymerization with respect to CN [16]. In addition, the right shift of the peripheral signal peak of CN-Mo_{0.2} may be due to the change of the connection environment of the tertiary N, which further confirms the successful doping of Mo(VI).

Fig. 5a reveals the steady state fluorescence emission spectra of all samples at 365 nm excitation light. Compared to CN, Mo-modified samples not only have a decrease in PL intensity but also a red shift in the maximum peak, the former corresponding to the suppressed electron-hole recombination rate and the latter due to the extended π -conjugated system [30]. The electronic configuration of Mo⁶⁺ is [Kr] 4d⁵5s¹, the successful doping of Mo(VI) significantly promotes the

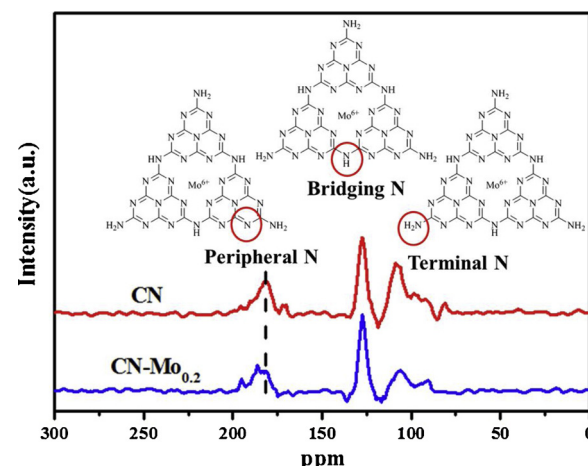


Fig. 4. ¹⁵N cross-polarization solid state NMR information of CN and CN-Mo_{0.2}.

mobility of the charge carriers due to the fact that the 4d orbit possesses characteristics of energy shallowness and non-localization compared with the 3d orbital [31].

Time-resolved fluorescence spectroscopy was used to further explore the promotion of Mo(VI) in photocatalytic activity. The fitted fluorescence decay lifetimes of CN and CN-Mo_{0.2} are shown in the Fig. 5b. Apparently, the corresponding percentage of the three different decay lifetimes of CN-Mo_{0.2} is significantly increased compared to the unmodified CN (Table S1), and the calculated average fluorescence lifetime is 1.4 times as high as that of CN. These results provide solid evidence for confirming that the modified sample has excellent charge carrier separation capabilities.

Electron paramagnetic resonance (EPR) was used to investigate the photogenerated charge generation capabilities of CN and CN-Mo_{0.2}. As can be seen in Fig. 5c, both materials have one independent Lorentz-derived line originated from the unpaired electronic signals of the carbon atoms on the heptazine ring [32]. More electrons are excited when the light is illuminated to the semiconductor, leading to materials to exhibit an enhanced EPR signal under visible light illumination.

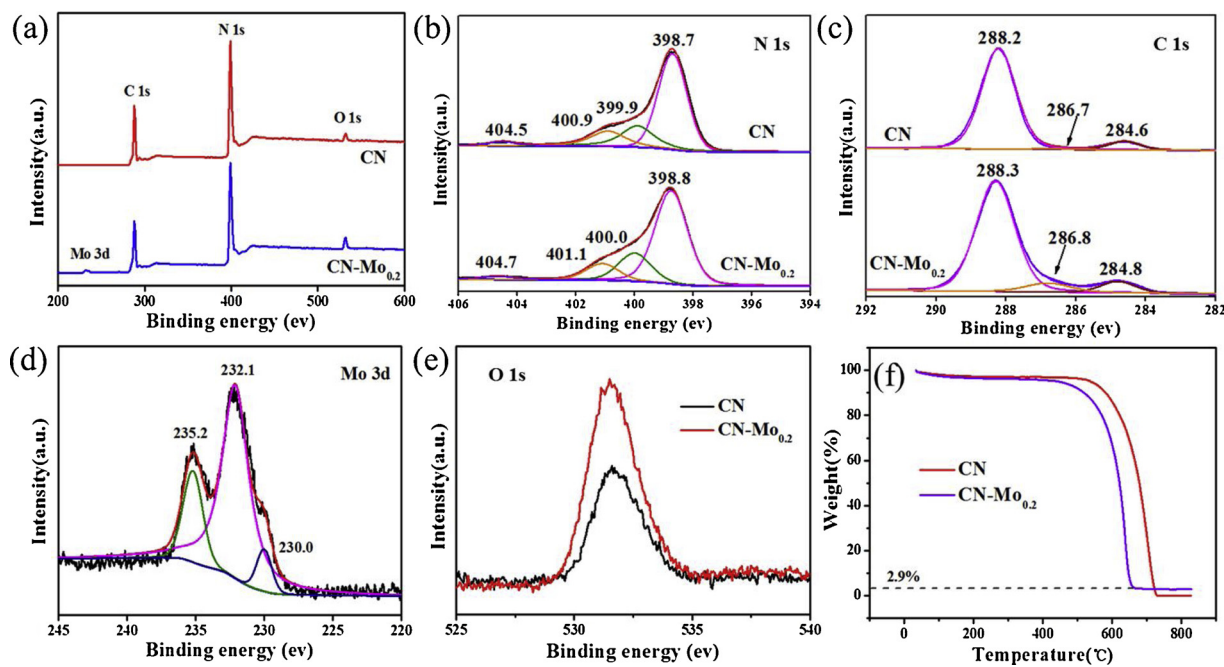


Fig. 3. (a) Survey XPS spectra; (b) N 1s; (c) C 1s; (d) high-resolution XPS spectra of Mo 3d; (e) O 1s high-resolution XPS spectra of CN and CN-Mo_{0.2}; (f) thermogravimetric curves for CN and CN-Mo_{0.2}.

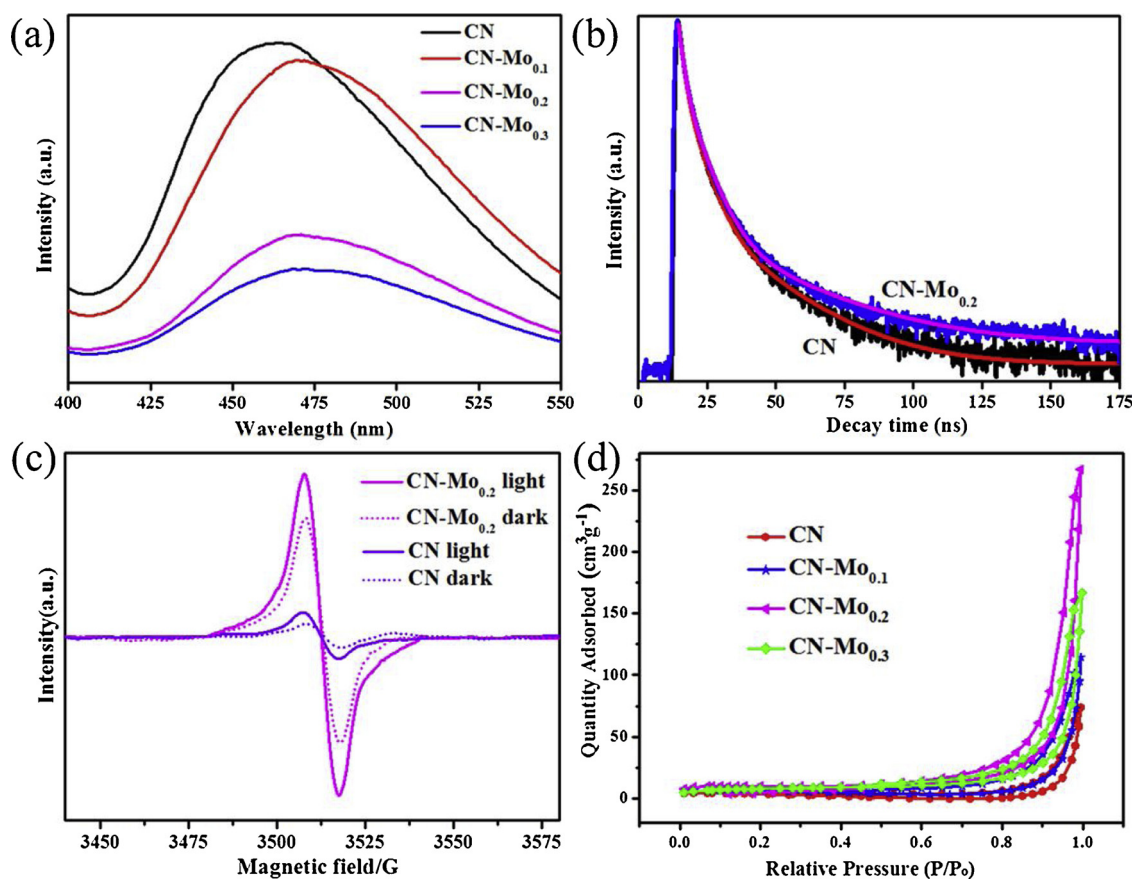


Fig. 5. (a) PL spectra of pristine CN, CN-Mo_{0.1}, CN-Mo_{0.2}, CN-Mo_{0.3}; (b) transient fluorescence decay of CN and CN-Mo_{0.2}; (c) EPR signal of CN and CN-Mo_{0.2} in light and darkness; (d) nitrogen adsorption-desorption isotherms of prepared materials.

However, CN-Mo_{0.2} exhibits an obviously enhanced derivative line signals compared to CN, which clearly indicates that CN-Mo_{0.2} has better electron delocalization ability than CN to generate more solitary electron pairs, thereby improving the photogenerated electron utilization and photocatalytic activities [33].

The N₂ isothermal adsorption-desorption curves (Fig. 5d) and pore size distributions (Fig. S3) of all samples were obtained to calculate the BET specific surface areas. The isotherms show typical IV curve, indicating the formation of mesopores and macropores in the materials [34]. Furthermore, H3 hysteresis loops are present at high relative pressures, representing the presence of slit-like pores, which may originate from irregular accumulation of nanorods or dendritic topography. Table S2 shows the specific surface area, pore diameter and pore volume of the obtained samples. The increased specific surface area means that there are more active sites which in turn promote the catalyst to exhibit enhanced catalytic activity.

Fig. 6 shows the transient reproducible photocurrent spectrum and electrochemical impedance spectroscopy (EIS) of materials obtained using chronoamperometry. Obviously, the photocurrent density of CN-Mo_x is much higher than that of CN (Fig. 6a), especially CN-Mo_{0.2}, its photocurrent density (1.35 μ A·cm⁻²) is 3.30 times as large as CN (0.47 μ A·cm⁻²), indicating that the samples of CN-Mo_x have stronger charge carrier separation ability and higher conductivity [35]. Meanwhile, the Nyquistarc diagram shows that the arc radius of Mo-doped catalysts is significantly reduced (Fig. 6b), inferring that CN-Mo_x have smaller charge transfer resistance than the bare CN [36]. The valence band (E_{VB}) and conduction band (E_{CB}) energy levels of the prepared materials were evaluated by ultraviolet photoelectron spectroscopy (UPS) and Mott-Schottky curves. The E_{VB} was obtained by subtracting the width of the He I UPS spectrum from the excitation energy (21.22 eV). Fig. 6c shows the width of the UPS at the edge of tangent,

the E_{VB} of CN, CN-Mo_{0.1}, CN-Mo_{0.2}, CN-Mo_{0.3} is calculated to be 6.35, 6.33, 6.28, 6.30 eV (vs vacuum level), respectively. According to the reference standard for which 0 versus RHE (reversible hydrogen electrode) equals to -4.44 eV versus vacuum level, the energy levels of E_{VB} (versus RHE) are calculated to be 1.91, 1.89, 1.84, 1.86 eV, respectively [37,38]. As shown in Fig. 6d, we obtained the flat band potentials of CN, CN-Mo_{0.1}, CN-Mo_{0.2}, CN-Mo_{0.3} versus the saturated calomel electrode (SCE) by tangential from Mott-Schottky plots. Above the flat band potential of 0.1 V, the E_{CB} (vs. SCE) of the samples are -1.16, -1.13, -1.09, -1.05 V, corresponding to -0.92, -0.89, -0.85, -0.81 eV relative to the normal hydrogen electrode (NHE), respectively [39,40]. The detailed positions of E_{VB} and E_{CB} for synthesized samples are depicted in Fig. S4. The narrowed band gap of the Mo-doped catalysts may be due to the formation of a new excitation conduction band during photocatalysis.

3.2. Photocatalytic activities

The sunlight was simulated by using a light source of $\lambda > 420$ nm to complete the hydrogen evolution reaction under visible light (Fig. 7a). The significant increase in the catalytic activity of CN-Mo_x reflects the superiority of the biotemplate method for the synthesis of Mo-doped g-C₃N₄, which can be attributed to the extended π - π conjugate and red-shifted of visible light absorption edge. More importantly, the increased specific surface area and self-assembled flower morphology provide a large number of exposed active sites for the reduction reaction, which accelerates the rate of hydrogen production. In particular, the hydrogen evolution rate of CN-Mo_{0.2} is as high as 2008.9 umol/g·h, which is about 9.6 times higher than that of CN (210.1 umol/g·h). The hydrogen evolution performance at $\lambda > 460$ nm shows that CN-Mo_{0.2} still has the best catalytic activity (Fig. 7b). As shown in

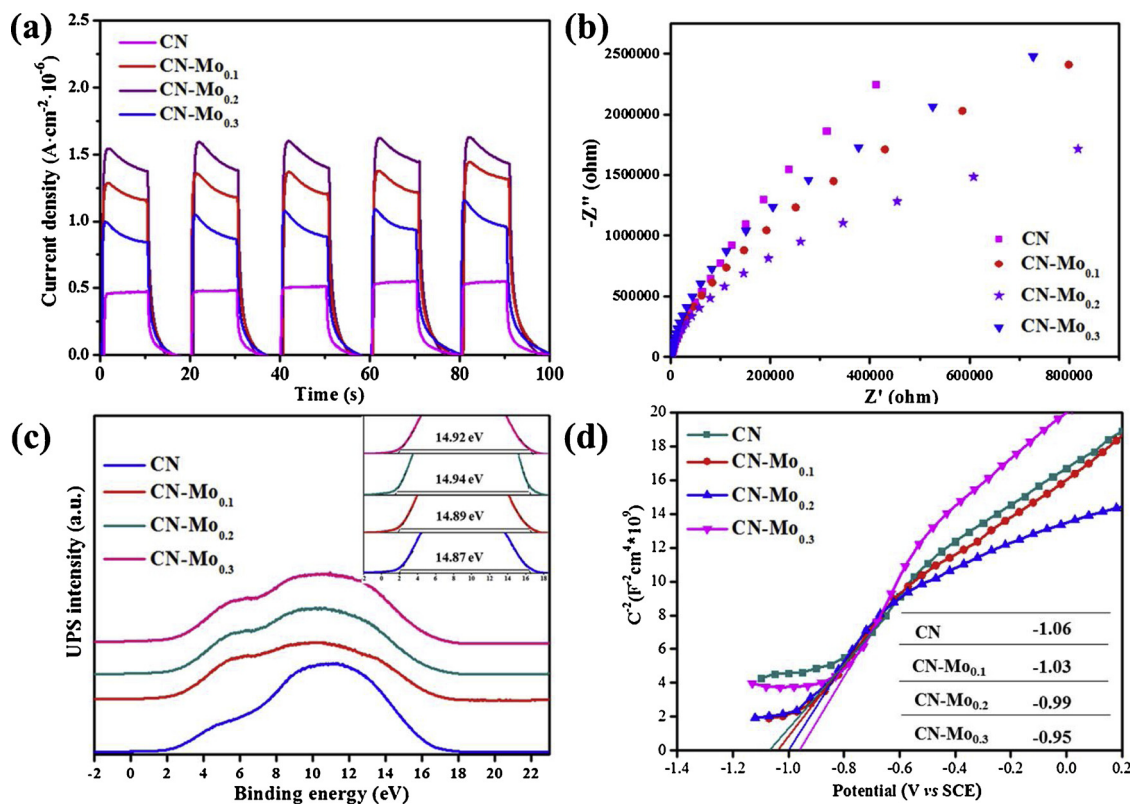


Fig. 6. (a) Transient photocurrent response curves; (b) EIS Nyquist plots for CN, CN-Mo_{0.1}, CN-Mo_{0.2}, CN-Mo_{0.3}; (c) UPS He I photoemission spectrum ($\hbar\nu = 21.22$ eV); (d) Mott-Schottky plots for synthesized samples.

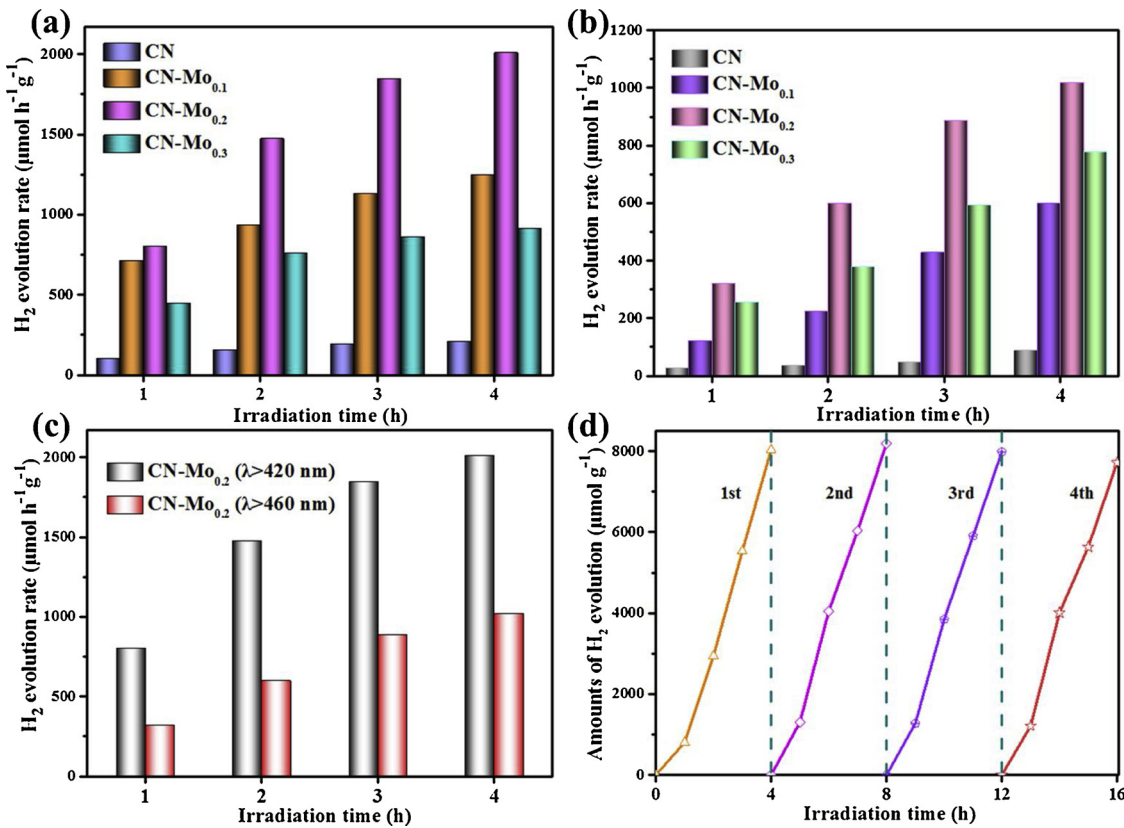


Fig. 7. Photocatalytic H₂ generation rate of the as-prepared photocatalysts under visible light irradiation (a) $\lambda > 420$ nm; (b) $\lambda > 460$ nm; (c) comparison of $\lambda > 420$ nm and $\lambda > 460$ nm; (d) recyclability performance of the optimal sample CN-Mo_{0.2}.

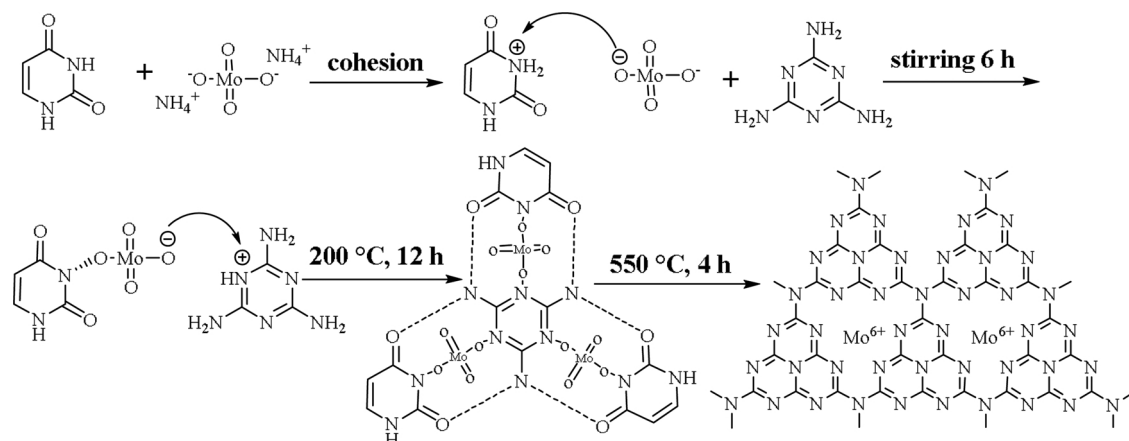
Table 2The comparison of activity of photocatalytic hydrogen evolution of CN-Mo_{0.2} with some reported g-C₃N₄-based photocatalysts.

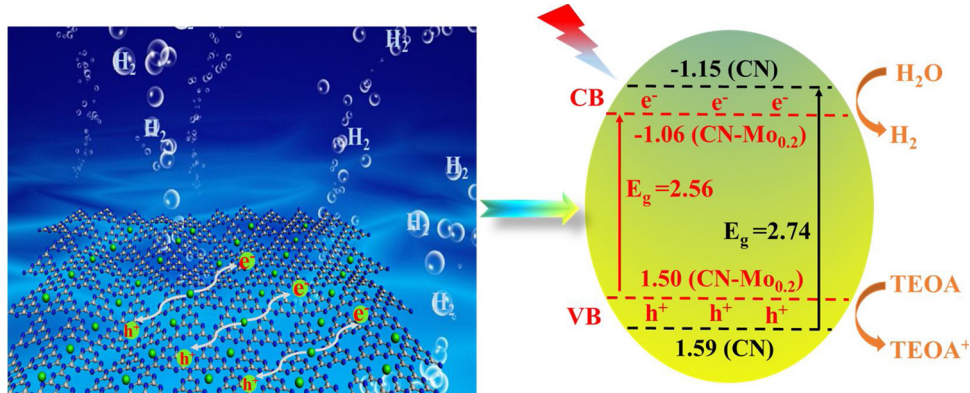
Photocatalyst	H ₂ (μmol h ⁻¹)	Amount (mg)	Incident light λ (nm)	H ₂ (μmol h ⁻¹ g ⁻¹)	Increased multiple	Reference
CoP/g-C ₃ N ₄	96.2	50	> 420	1924	3.0	[19]
C-rich g-C ₃ N ₄	8.6	10	> 420	860	86.0	[41]
P/g-C ₃ N ₄	11.4	20	> 400	571	13.3	[42]
Fe-doped g-C ₃ N ₄	53.6	100	≥ 420	536	6.0	[43]
O-doped g-C ₃ N ₄	18.3	25	> 420	732	5.7	[27]
K-doped g-C ₃ N ₄	66.9	50	≥ 400	1337	5.6	[18]
Br-modified g-C ₃ N ₄	48.0	50	> 420	960	2.4	[44]
CN-10	22.9	50	≥ 420	459	5.2	[45]
Pt/meso-S2	41.0	50	≥ 420	820	8.2	[46]
HC-CN	80.8	100	≥ 400	808	20.0	[47]
Al-aa(0.32%)_PCN	59.1	50	> 420	1182	3.9	[22]
CCN-1	52.9	100	> 420	529	6.7	[48]
(P, Mo)-g-C ₃ N _x	1.2	10	> 420	120	/	[31]
CN-Mo_{0.2}	100.4	50	≥ 420	2009	9.6	This work

Fig. 7c, the hydrogen evolution rate of CN-Mo_{0.2} decreases as the increase of incident light wavelength, representing that the photo-responsibility of the material is weakened when $\lambda > 460$ nm, which is consistent with **Fig. 1d**. In addition, AQE of the prepared materials at different wavelengths is shown in Table S3. The stability of CN-Mo_{0.2} was evaluated by means of uninterrupted photocatalytic hydrogen evolution for 16 h. As shown in **Fig. 7d**, there is no unpredictable decrease in the hydrogen evolution rate of CN-Mo_{0.2} after four consecutive cycles. Moreover, the XRD patterns (Fig. S5) and FT-IR spectrum (Fig. S6) before and after cycle test show that there is no significant change in the skeleton structure of g-C₃N₄, representing that the material has high structural stability and good sustainable utilization. Apart from the above characterization, we attempt to correlate the photocatalytic performance of CN-Mo_{0.2} with previously reported g-C₃N₄-based photocatalysts. Clearly, the inclusion of various catalysts is a relatively difficult task because of the different reaction conditions and chemical compositions. Therefore, relevance must be treated with caution. Nevertheless, CN-Mo_{0.2} can still exhibit certain advantages in photocatalytic activity. The results in **Table 2** further illustrate that the biotemplate method plays an active role in the photocatalytic reaction of CN-Mo_{0.2}.

3.3. Chelation-hydrogen bond coordination mechanism

Although little work has been done on Mo-doped g-C₃N₄, many articles relating to the doping of elements such as P, S, Na and Se have been reported [14,20,49,50]. Based on a large number of literatures and previous characterization results, we proposed a hypothetical mechanism for the bio-template synthesis of Mo-doped g-C₃N₄, as shown in **scheme 2**.

**Scheme 2.** Schematic diagram of molecular interactions during the synthesis of Mo-doped g-C₃N₄.



Scheme 3. Schematic diagram of photo-excited electron-hole separation and transport process occurring on CN-Mo_{0.2} under visible light irradiation.

3.4. Photocatalytic reaction mechanism

In summary, Mo-doped g-C₃N₄ exhibits the following advantages in the photocatalytic process: (1) The introduction of uracil provides the chelate template and self-assembled microenvironment for the formation of intermediates, in addition to expanded π - π conjugation, the specific surface area is also increased. (2) The formation of the built-in electric field of the electron donor-receptor in the chelate facilitates the delocalization of photoexcited electrons (Figs. 5c and 6a), reducing the transmission impedance of electrons (Fig. 6b), ensuring effective separation and transfer of photogenerated carriers. (3) Mo-doped g-C₃N₄ constructs a more suitable CB and a narrower E_g at a lower energy level because of the non-localized nature of Mo(VI), which better satisfies the conditions of the reduction reaction and expands the response range to visible light (Scheme 3).

4. Conclusions

Mo-doped g-C₃N₄ with different morphologies was successfully prepared by biological template method. As a result, the synthesized samples exhibited an increased specific surface area, enhanced visible light absorption, reduced electron-hole recombination rate, and improved photocatalytic activity. Finally, the chelation-hydrogen bond coordination mechanism was proposed based on the detailed analysis results. The rational design and successful preparation of highly efficient Mo-doped g-C₃N₄ provides a new approach to the development and construction of catalysts for other potential transition elements.

Acknowledgments

This work was supported by the financial supports of the National Natural Science Foundation of China (Grant No. 21878047, 21676056 and 51673040), “Six Talents Pinnacle Program” of Jiangsu Province of China (JNHB-006), Qing Lan Project of Jiangsu Province (1107040167), Graduate student scientific research innovation program of Jiangsu Province (KYCX18_0132), Scientific Research Foundation of Graduate School of Southeast University (YBPY1880) and A Project Funded by the Priority Academic Program Development of Jiangsu Higher Education Institutions (PAPD) (1107047002).

Appendix A. Supplementary data

Supplementary material related to this article can be found, in the online version, at doi:<https://doi.org/10.1016/j.apcatb.2019.02.007>.

References

- Z. Zhao, G. Ge, D. Zhang, Heteroatom-doped carbonaceous photocatalysts for solar fuel production and environmental remediation, *ChemCatChem* 10 (2018) 62–123.
- S. Zhao, Y. Zhang, Y. Wang, Y. Zhou, K. Qiu, C. Zhang, J. Fang, X. Sheng, Ionic liquid-assisted synthesis of Br-modified g-C₃N₄ semiconductors with high surface area and highly porous structure for photoredox water splitting, *J. Power Sources* 370 (2017) 106–113.
- W.J. Ong, L.L. Tan, Y.H. Ng, S.T. Yong, S.P. Chai, Graphitic carbon nitride (g-C₃N₄)-based photocatalysts for artificial photosynthesis and environmental remediation: are we a step closer to achieving sustainability? *Chem. Rev.* 116 (2016) 7159–7329.
- Y.-Y. Han, X.-L. Lu, S.-F. Tang, X.-P. Yin, Z.-W. Wei, T.-B. Lu, Metal-free 2D/2D heterojunction of graphitic carbon nitride/graphdiyne for improving the hole mobility of graphitic carbon nitride, *Adv. Energy Mater.* 8 (2018) 1702992.
- M. Wu, J. Zhang, B.-b. He, H.-w. Wang, R. Wang, Y.-s. Gong, In-situ construction of coral-like porous P-doped g-C₃N₄ tubes with hybrid 1D/2D architecture and high efficient photocatalytic hydrogen evolution, *Appl. Catal. B: Environ.* 241 (2019) 159–166.
- Z. Jiang, W. Wan, H. Li, S. Yuan, H. Zhao, P.K. Wong, A hierarchical Z-scheme α -Fe₂O₃/g-C₃N₄ hybrid for enhanced photocatalytic CO₂ reduction, *Adv. Mater.* 30 (2018) 1706108.
- Y. Wang, W. Yang, X. Chen, J. Wang, Y. Zhu, Photocatalytic activity enhancement of core-shell structure g-C₃N₄@TiO₂ via controlled ultrathin g-C₃N₄ layer, *Appl. Catal. B: Environ.* 220 (2018) 337–347.
- C. Liu, H. Huang, W. Cui, F. Dong, Y. Zhang, Band structure engineering and efficient charge transport in oxygen substituted g-C₃N₄ for superior photocatalytic hydrogen evolution, *Appl. Catal. B: Environ.* 230 (2018) 115–124.
- H. Che, L. Liu, G. Che, H. Dong, C. Liu, C. Li, Control of energy band, layer structure and vacancy defect of graphitic carbon nitride by intercalated hydrogen bond effect of NO₃⁻ toward improving photocatalytic performance, *Chem. Eng. J.* 357 (2019) 209–219.
- Y. Hu, Y. Wu, J. Wang, Manganese-oxide-based electrode materials for energy storage applications: how close are we to the theoretical capacitance? *Adv. Mater.* 30 (2018) 1802569.
- F. Pu, J. Ren, X. Qu, Nucleobases, nucleosides, and nucleotides: versatile biomolecules for generating functional nanomaterials, *Chem. Soc. Rev.* 47 (2018) 1285–1306.
- Y. Zhang, L. Wu, X. Zhao, Y. Zhao, H. Tan, X. Zhao, Y. Ma, Z. Zhao, S. Song, Y. Wang, Y. Li, Leaf-mosaic-inspired vine-like graphitic carbon nitride showing high light absorption and efficient photocatalytic hydrogen evolution, *Adv. Energy Mater.* 8 (2018) 1801139.
- Y. Wang, S. Zhao, Y. Zhang, J. Fang, W. Chen, S. Yuan, Y. Zhou, Facile synthesis of self-assembled g-C₃N₄ with abundant nitrogen defects for photocatalytic hydrogen evolution, *ACS Sustain. Chem. Eng.* 6 (2018) 10200–10210.
- L. Zhang, N. Ding, M. Hashimoto, K. Iwasaki, N. Chikamori, K. Nakata, Y. Xu, J. Shi, H. Wu, Y. Luo, D. Li, A. Fujishima, Q. Meng, Sodium-doped carbon nitride nanotubes for efficient visible light-driven hydrogen production, *Nano Res.* 11 (2018) 2295–2309.
- S. Zhao, Y. Zhang, Y. Zhou, Y. Wang, K. Qiu, C. Zhang, J. Fang, X. Sheng, Facile one-step synthesis of hollow mesoporous g-C₃N₄ spheres with ultrathin nanosheets for photoredox water splitting, *Carbon* 126 (2018) 247–256.
- C.-Y. Hsu, K.-S. Chang, Fabrication and photocatalytic application of aromatic ring functionalized melamine oligomers, *J. Phys. Chem. C* 122 (2018) 3506–3512.
- F.J. Maldonado-Hodar, H. Jirglová, S. Morales-Torres, A.F. Pérez-Cadenas, Influence of surfactants on the physicochemical properties and catalytic behaviour of Mo-doped carbon xerogels, *Catal. Today* 301 (2018) 217–225.
- Y. Wang, S. Zhao, Y. Zhang, J. Fang, Y. Zhou, S. Yuan, C. Zhang, W. Chen, One-pot synthesis of K-doped g-C₃N₄ nanosheets with enhanced photocatalytic hydrogen production under visible-light irradiation, *Appl. Surf. Sci.* 440 (2018) 258–265.
- C. Li, Y. Du, D. Wang, S. Yin, W. Tu, Z. Chen, M. Kraft, G. Chen, R. Xu, Unique P-Co-N surface bonding states constructed on g-C₃N₄ nanosheets for drastically enhanced photocatalytic activity of H₂ evolution, *Adv. Funct. Mater.* 27 (2017) 1604328.
- H. Yang, Y. Zhou, Y. Wang, S. Hu, B. Wang, Q. Liao, H. Li, J. Bao, G. Ge, S. Jia, Three-dimensional flower-like phosphorus-doped g-C₃N₄ with a high surface area for visible-light photocatalytic hydrogen evolution, *J. Mater. Chem. A* 6 (2018) 16485–16494.
- S. Gong, Z. Jiang, P. Shi, J. Fan, Q. Xu, Y. Min, Noble-metal-free heterostructure for efficient hydrogen evolution in visible region: molybdenum nitride/ultrathin

graphitic carbon nitride, *Appl. Catal. B: Environ.* 238 (2018) 318–327.

[22] C.H. Choi, L. Lin, S. Gim, S. Lee, H. Kim, X. Wang, W. Choi, Polymeric carbon nitride with localized aluminum coordination sites as a durable and efficient photocatalyst for visible light utilization, *ACS Catal.* 8 (2018) 4241–4256.

[23] C. Guan, W. Xiao, H. Wu, X. Liu, W. Zang, H. Zhang, J. Ding, Y.P. Feng, S.J. Pennycook, J. Wang, Hollow Mo-doped CoP nanoarrays for efficient overall water splitting, *Nano Energy* 48 (2018) 73–80.

[24] R. Alipour Moghadam Esfahani, L.M. Rivera Gavidia, G. García, E. Pastor, S. Specchia, Highly active platinum supported on Mo-doped titanium nanotubes suboxide (Pt/TNTS-Mo) electrocatalyst for oxygen reduction reaction in PEMFC, *Renew. Energy* 120 (2018) 209–219.

[25] G. Bai, X. Lan, X. Liu, C. Liu, L. Shi, Q. Chen, G. Chen, An ammonium molybdate deposited amorphous silica coated iron oxide magnetic core-shell nanocomposite for the efficient synthesis of 2-benzimidazoles using hydrogen peroxide, *Green Chem.* 16 (2014) 3160–3168.

[26] Y. Chen, C. Dong, J. Zhang, C. Zhang, Z. Zhang, Hierarchically porous Mo-doped Ni₂O₃ nanowires efficiently catalyzing oxygen/hydrogen evolution reactions, *J. Mater. Chem. A* 6 (2018) 8430–8440.

[27] Y. Zeng, X. Liu, C. Liu, L. Wang, Y. Xia, S. Zhang, S. Luo, Y. Pei, Scalable one-step production of porous oxygen-doped g-C₃N₄ nanorods with effective electron separation for excellent visible-light photocatalytic activity, *Appl. Catal. B: Environ.* 224 (2018) 1–9.

[28] V.W.-h. Lau, M.B. Mesch, V. Duppel, V. Blum, J. Senker, B.V. Lotsch, Low-molecular-weight carbon nitrides for solar hydrogen evolution, *J. Am. Chem. Soc.* 137 (2015) 1064–1072.

[29] S. Wu, S. Wen, X. Xu, G. Huang, Y. Cui, J. Li, A. Qu, Facile synthesis of porous graphene-like carbon nitride nanosheets with high surface area and enhanced photocatalytic activity via one-step catalyst-free solution self-polymerization, *Appl. Surf. Sci.* 436 (2018) 424–432.

[30] Y. Wang, S. Zhao, Y. Zhang, W. Chen, S. Yuan, Y. Zhou, Z. Huang, Synthesis of graphitic carbon nitride with large specific surface area via copolymerizing with nucleobases for photocatalytic hydrogen generation, *Appl. Surf. Sci.* 463 (2019) 1–8.

[31] D. Chen, J. Liu, Z. Jia, J. Fang, F. Yang, Y. Tang, K. Wu, Z. Liu, Z. Fang, Efficient visible-light-driven hydrogen evolution and Cr(VI) reduction over porous P and Mo co-doped g-C₃N₄ with feeble N vacancies photocatalyst, *J. Hazard. Mater.* 361 (2019) 294–304.

[32] E.S. Da Silva, N.M.M. Moura, A. Coutinho, G. Drazic, B.M.S. Teixeira, N.A. Sobolev, C.G. Silva, M. Neves, M. Prieto, J.L. Faria, β-cyclodextrin as a precursor to holey C-doped g-C₃N₄ nanosheets for photocatalytic hydrogen generation, *ChemSusChem* 11 (2018) 2681–2694.

[33] X. Wang, Q. Liu, Q. Yang, Z. Zhang, X. Fang, Three-dimensional g-C₃N₄ aggregates of hollow bubbles with high photocatalytic degradation of tetracycline, *Carbon* 136 (2018) 103–112.

[34] S. Zhao, Y. Zhang, J. Fang, H. Zhang, Y. Wang, Y. Zhou, W. Chen, C. Zhang, Self-assembled mesoporous carbon nitride with tunable texture for enhanced visible-light photocatalytic hydrogen evolution, *ACS Sustain. Chem. Eng.* 6 (2018) 8291–8299.

[35] R. Shen, J. Xie, P. Guo, L. Chen, X. Chen, X. Li, Bridging the g-C₃N₄ nanosheets and robust CuS cocatalysts by metallic acetylene black interface mediators for active and durable photocatalytic H₂ production, *ACS Appl. Energy Mater.* 1 (2018) 2232–2241.

[36] W. Chen, J. Pei, C.T. He, J. Wan, H. Ren, Y. Zhu, Y. Wang, J. Dong, S. Tian, W.C. Cheong, S. Lu, L. Zheng, X. Zheng, W. Yan, Z. Zhuang, C. Chen, Q. Peng, D. Wang, Y. Li, Rational design of single molybdenum atoms anchored on N-doped carbon for effective hydrogen evolution reaction, *Angew. Chem.* 56 (2017) 16086–16090.

[37] Y. Shang, G. Li, W. Liu, Z. Ning, Quasi-2D inorganic CsPbBr₃ perovskite for efficient and stable light-emitting diodes, *Adv. Funct. Mater.* 28 (2018) 1801193.

[38] Z. Mao, J. Chen, Y. Yang, L. Bie, B.D. Fahlman, D. Wang, Modification of surface properties and enhancement of photocatalytic performance for g-C₃N₄ via plasma treatment, *Carbon* 123 (2017) 651–659.

[39] C. Liang, L. Zhang, H. Guo, C.-G. Niu, X.-J. Wen, N. Tang, H.-Y. Liu, Y.-Y. Yang, B.-B. Shao, G.-M. Zeng, Photo-removal of 2,2'4,4'-tetrabromodiphenyl ether in liquid medium by reduced graphene oxide bridged artificial Z-scheme system of Ag@Ag₃PO₄/g-C₃N₄, *Chem. Eng. J.* 361 (2019) 373–386.

[40] N. Tian, Y. Zhang, X. Li, K. Xiao, X. Du, F. Dong, G.I.N. Waterhouse, T. Zhang, H. Huang, Precursor-reforming protocol to 3D mesoporous g-C₃N₄ established by ultrathin self-doped nanosheets for superior hydrogen evolution, *Nano Energy* 38 (2017) 72–81.

[41] Y. Li, M. Yang, Y. Xing, X. Liu, Y. Yang, X. Wang, S. Song, Preparation of carbon-rich g-C₃N₄ nanosheets with enhanced visible light utilization for efficient photocatalytic hydrogen production, *Small* 13 (2017) 1701552.

[42] J. Ran, W. Guo, H. Wang, B. Zhu, J. Yu, S.Z. Qiao, Metal-free 2D/2D phosphorene/g-C₃N₄ van der waals heterojunction for highly enhanced visible-light photocatalytic H₂ production, *Adv. Mater.* 30 (2018) 1800128.

[43] J. Gao, Y. Wang, S. Zhou, W. Lin, Y. Kong, A facile one-step synthesis of Fe-doped g-C₃N₄ nanosheets and their improved visible-light photocatalytic performance, *ChemCatChem* 9 (2017) 1708–1715.

[44] Z.-A. Lan, G. Zhang, X. Wang, A facile synthesis of Br-modified g-C₃N₄ semiconductors for photoredox water splitting, *Appl. Catal. B: Environ.* 192 (2016) 116–125.

[45] F. Yang, D. Liu, Y. Li, L. Cheng, J. Ye, Salt-template-assisted construction of honeycomb-like structured g-C₃N₄ with tunable band structure for enhanced photocatalytic H₂ production, *Appl. Catal. B: Environ.* 240 (2019) 64–71.

[46] X. Liu, F. Pang, M. He, J. Ge, Confined reaction inside nanotubes: new approach to mesoporous g-C₃N₄ photocatalysts, *Nano Res.* 10 (2017) 3638–3647.

[47] F. Xing, W. Tu, Z. Han, Y. Hu, Q. Meng, G. Chen, Template-induced high-crystalline g-C₃N₄ nanosheets for enhanced photocatalytic H₂ evolution, *ACS Energy Lett.* 3 (2018) 514–519.

[48] H. Li, F. Li, Z. Wang, Y. Jiao, Y. Liu, P. Wang, X. Zhang, X. Qin, Y. Dai, B. Huang, Fabrication of carbon bridged g-C₃N₄ through supramolecular self-assembly for enhanced photocatalytic hydrogen evolution, *Appl. Catal. B: Environ.* 229 (2018) 114–120.

[49] Y. Wang, Y. Tian, L. Yan, Z. Su, DFT study on sulfur-doped g-C₃N₄ nanosheets as a photocatalyst for CO₂ reduction reaction, *J. Phys. Chem. C* 122 (2018) 7712–7719.

[50] A. Kumar, R.K. Yadav, N.-J. Park, J.-O. Baeg, Facile one-pot two-step synthesis of novel *in situ* selenium-doped carbon nitride nanosheet photocatalysts for highly enhanced solar fuel production from CO₂, *ACS Appl. Nano Mater.* 1 (2018) 47–54.

[51] J. Baillet, V. Desvergne, A. Hamoud, L. Latxague, P. Barthelemy, Lipid and nucleic acid chemistries: combining the best of both worlds to construct advanced biomaterials, *Adv. Mater.* 30 (2018) 1705078.

[52] P. Li, F. Wang, S. Wei, X. Li, Y. Zhou, Mechanistic insights into CO₂ reduction on Cu/Mo-loaded two-dimensional g-C₃N₄(001), *Phys. Chem. Chem. Phys.* 19 (2017) 4405–4410.